J. Fluid Mech. (1989), *vol.* 200, *pp.* 121–148
Printed in Great Britain

Transient flow in a side-heated cavity at high Rayleigh number: a numerical study

By S. G. SCHLADOW†, J. C. PATTERSON‡ AND R. L. STREET†

† Environmental Fluid Mechanics Laboratory, Department of Civil Engineering,
Stanford University, Stanford, CA 94305–4020, USA

‡ Center for Water Research, University of Western Australia, Nedlands, WA 6009, Australia

(Received 23 January 1988 and in revised form 16 June 1988)

A series of two- and three-dimensional numerical simulations of transient flow in a side-heated cavity has been conducted. The motivation for the work has been to resolve discrepancies between a flow description based on scaling arguments and one based on laboratory experiments, and to provide a more detailed description of the approach to steady state. All simulations were for a Rayleigh number of 2×10^9, and a water-filled cavity of aspect ratio 1. The simulations (beginning with an isothermal fluid at rest) generally agree with the results of the scaling arguments. In addition, the experimental observations are entirely accounted for by the position of the measurement instruments and the presence of an extremely weak, stabilizing temperature gradient in the vertical.

1. Introduction

Transient behaviour in fluid flow is of fundamental interest. Its investigation, however, presents problems particularly where the approach to steady state involves a multiplicity of time and length scales. For laboratory experiments these problems relate primarily to physical limitations, including design of an experiment that can satisfactorily approach the desired boundary and initial conditions, and choice of what and where to measure in an evolving flow. The problems are so severe that only relatively few transient flow experiments have been conducted. From the standpoint of numerical simulation the difficulties associated with measurements are trivial. On the other hand, producing a stable, accurate and efficient code to encompass the appropriate time and lengthscales is difficult. Therefore the approach taken in this paper is to use a numerical code, but one for which past experience in simulating unsteady flows provides a basis for confidence in its accuracy.

The transient flow considered is that arising in a square cavity across which a temperature difference is imposed. The three dimensionless parameters that describe such a flow are the Rayleigh number, the Prandtl number, and the aspect ratio of the cavity (Batchelor 1954). Patterson & Imberger (1980) used scaling arguments to derive a classification scheme based on the relative values of groupings of these dimensionless parameters. Using this scheme, features of the transient behaviour could be described and applicable time and lengthscales calculated. For lower Rayleigh number flows, numerical simulations supported their classification. In their regime V, the classification scheme suggested the existence of internal wave motions. Physical experiments by Yewell, Poulikakos & Bejan (1982) were directed towards this regime and confirmed some aspects of the flow; however, the expected oscillating approach to steady state at higher Rayleigh numbers was not observed. It was subsequently shown by Patterson (1984) that these experiments were in fact conducted in a non-oscillatory regime and were, accordingly, consistent with the classification scheme.

More recently, Ivey (1984) conducted an experiment in a range for which the classification did indeed suggest oscillations would be present. Three of his observations are particularly noteworthy and provided the impetus for the present work. First, he did not observe the seiching-type motion suggested by Patterson & Imberger, although oscillations were present in part of the cavity. Second, there was a large core motion that rotated counter to the main flow in the boundaries – essentially in a direction that was down the hot wall and up the cold wall. This was evident only in the early stages of the flow and was not present as the flow advanced towards steady state. Third, there were 'hydraulic jump-like' features present on the horizontal boundaries near the top of the hot wall and the bottom of the cold wall.

The present work describes a series of numerical simulations, based on one of the flow cases investigate by Ivey (1984). The adopted reference is the 'ideal' of a two-dimensional square cavity initially containing isothermal water at rest. At time zero, one vertical sidewall is heated and the opposite one cooled by equivalent temperature differences, and thereafter this difference is maintained. To test the sensitivity of the flow we have introduced a number of variations from this ideal. The changes are of a type and magnitude that could be present in a laboratory experiment, and include gradually heated sidewalls, non-insulated upper and lower boundaries, allowance for three-dimensional motions, and an initial vertical temperature gradient in the cavity. The first three variations represent in part the conditions of the experiments described by Ivey (1984). The existence of a vertical temperature gradient was not ascertained in those experiments, and so its existence is purely speculative.

2. Simulation codes

The numerical results were obtained using the REMIXCS code (Freitas *et al.* 1985) and a major modification to it, the SEAFLOS1 code (Perng & Street 1988). Both solve the Navier–Stokes and energy equations in primitive variables on a non-uniform, two- or three-dimensional mesh. The difference equations are derived by volume integration of the partial differential equations on a control volume surrounding each node of the space-staggered computational mesh. A quadratic upstream interpolation technique (QUICK) is used in the finite-difference formulation of the convective terms to produce a numerical scheme that is globally second-order accurate in space (Leonard 1979). A backward-Euler (implicit, first-order-accurate) time-differencing scheme is used to step the calculation forward in time. The Boussinesq assumption is only partially invoked (i.e. the temporal variation of density is assumed negligible), and fluid properties (density, viscosity, specific heat and thermal conductivity) are dynamically computed as functions of temperature. While the former code is based on the long established SIMPLE algorithm (Patankar 1980), SEAFLOS1 incorporates a number of significant changes. An exact pressure equation is now solved (in a method similar to the PRIME algorithm of Van Doormaal & Raithby 1984). By using the Incomplete Cholesky Decomposition–Conjugate Gradient method for solving this equation, the speed was enhanced by a factor of 5. A revised QUICK formulation for non-uniform grids is included, as are refinements to the treatment of the boundary conditions.

Both codes have been used successfully to simulate lid-driven cavity flows. Freitas *et al.* (1985) used REMIXCS at a Reynolds number of 3200 and reproduced experimentally observed Taylor–Görtler-like vortices and other three-dimensional features heretofore not simulated. Even better agreement for the same flow has since been attained by using the SEAFLOS1 code (Perng & Street 1988; Prasad, Perng & Koseff, 1988).

Several versions of SEAFLOS1 and REMIXCS have been used to examine the present problem. Although slight differences exist between each result (many used different mesh spacings) the basic flow structure produced was unchanged. The results to be presented are all from the SEAFLOS1 code.

3. Scaling of the flow and considerations of vorticity

The scaling arguments of Patterson & Imberger (1980) provide a theoretical description of the flow structure that, for the case to be presented, has yet to be fully tested. In this case, the nominal parameter values are Rayleigh number, $Ra = 2\times 10^9$, Prandtl number, $\sigma = 7.1$ and aspect ratio, $A = 1$. This corresponds to an ambient temperature of 20 °C and sidewall temperatures of 15 and 25 °C in a cavity of height 0.24 m, as shown in figure 1 (*a*). In the context of Patterson & Imberger we operate in the range of regime V ($A^{-6} < \sigma$ and $\sigma^{10} < Ra < \sigma^{16}A^{-12}$).

By their arguments, a double-layer structure starts to form on the vertical walls immediately after the temperature difference is imposed. The timescale for the growth of the inner thermal boundary layer is

$$\tau \sim \frac{h^2}{\kappa Ra^{\frac{1}{2}}}, \tag{1}$$

at which time the velocity and lengthscales are

$$V_T \sim \frac{\kappa Ra^{\frac{1}{2}}}{h}, \tag{2}$$

and

$$\delta_T \sim \frac{h}{Ra^{\frac{1}{4}}}. \tag{3}$$

Here h is the cavity height, κ the thermal diffusivity, the Rayleigh number is defined by $Ra = 2g\alpha\Delta T h^3/\nu\kappa$, the Prandtl number by $\sigma = \nu/\kappa$, where ν is the kinematic viscosity, $2\Delta T$ is the total temperature difference across the cavity, α is the coefficient of thermal expansion and g is the gravitational acceleration. For a square cavity, the aspect ratio $A = h/l = h/h = 1$. For Prandtl number, $\sigma > 1$, the lengthscale for the outer viscous layer is given by

$$\delta_\nu \sim \sigma^{\frac{1}{2}}\delta_T. \tag{4}$$

As the flow along the vertical walls approaches the corner, it is forced to discharge into the core of the cavity. For times greater than τ the unheated fluid from the viscous layer discharges as a potential flow, while the heated (cooled) fluid intrudes as a layer across the top (bottom) of the cavity. For sufficiently small times, the intruding layer is described by an inertia–buoyancy balance, suggesting a layer thickness of order

$$\Delta_g \sim \frac{h}{\sigma^{\frac{1}{3}}Ra^{\frac{1}{6}}}. \tag{5}$$

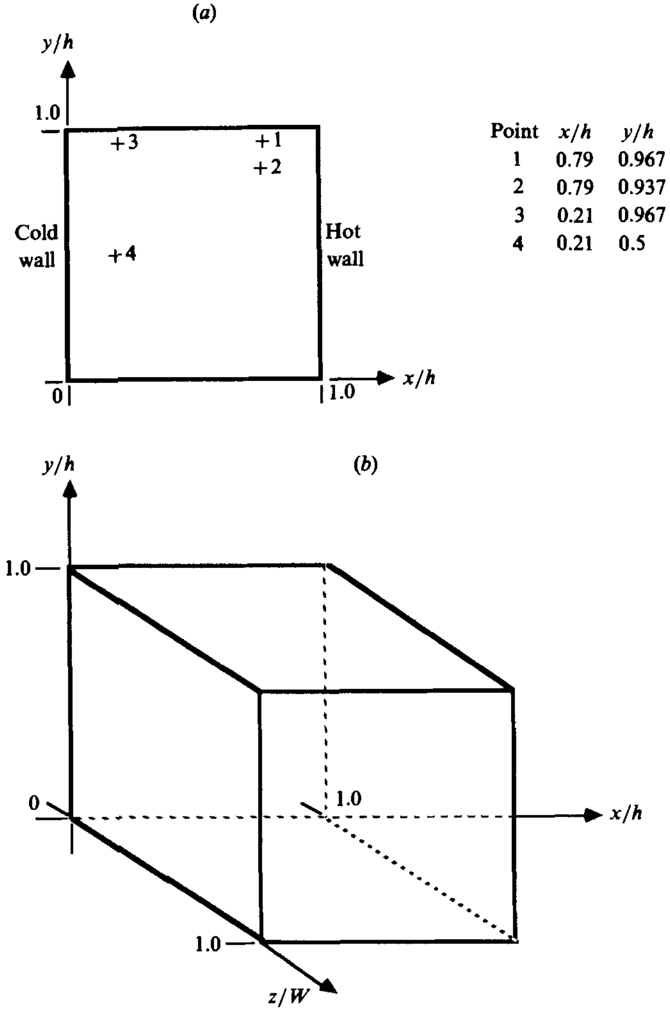

Point	x/h	y/h
1	0.79	0.967
2	0.79	0.937
3	0.21	0.967
4	0.21	0.5

FIGURE 1. General arrangement of simulated cavity. Dimensions are normalized by cavity dimensions (0.24 m in x- and y-directions, 0.2 m in z-direction). (*a*) Two-dimensional cavity. Points numbered 1–3 are locations of temperature probes in Ivey (1984) experiments. (*b*) Three-dimensional cavity.

The viscous terms become important at time of order

$$T_\nu \sim \frac{h^2}{\kappa \sigma^{\frac{5}{3}} Ra^{\frac{1}{3}}}, \tag{6}$$

after which a viscous–buoyancy balance suggests a growing intrusion thickness of order

$$\Delta_\nu \sim \frac{\kappa^{\frac{1}{5}} h^{\frac{3}{5}} t^{\frac{1}{5}}}{Ra^{\frac{1}{10}}}. \tag{7}$$

The velocity of the intrusion would be of order

$$U_g \sim \frac{V_T \delta_T}{\Delta}, \tag{8}$$

where Δ could be either of Δ_g or Δ_ν. For the parameter range inherent in regime V (Patterson & Imberger 1980), the scaling suggests that the transition from a buoyancy–inertia intrusion to a viscous–buoyancy intrusion occurs after the vertical boundary layer is established, but before an inertial intrusion could reach the opposite wall.

As horizontal intrusions continue to convect heat across the cavity there is a gradual filling of the core with a stable vertical temperature gradient. Filling occurs in the time taken for all the fluid in the cavity to pass through the thermal boundary layer, which is of order

$$T_{\mathrm{f}} \sim \frac{hl}{\kappa Ra^{\frac{1}{4}}}. \tag{9}$$

(Of course, here $l = h$ since $A = 1$.) At the same time, tilting of the isotherms owing to a 'piling up' of the intruding flow at the opposite side of the cavity may induce cavity-scale internal waves (seiches) of frequency

$$f \sim \frac{N}{(1+A^{-2})^{\frac{1}{2}}}, \tag{10}$$

where N is the Brunt–Väisälä frequency given by

$$N \sim \frac{(\nu\kappa Ra)^{\frac{1}{2}}}{h^2}. \tag{11}$$

The timescale for the decay of the wave motion is given by

$$T_{\mathrm{d}} \sim \frac{h^2}{\nu}, \tag{12}$$

and hence the time to steady state will be the larger of T_{f} or T_{d}.

The suggestion of a counter-rotating core and a jump-like structure and its associated small-scale circulating regions by the Ivey experiments indicate that the flow development may, at least in part, be best described in terms of the production and transport of vorticity. The scaling can readily be extended to encompass such an approach.

Consider, first, the vorticity generation mechanisms. The transport of vorticity is described in two dimensions by

$$\frac{\partial\omega}{\partial t}+\frac{u\,\partial\omega}{\partial x}+\frac{v\,\partial\omega}{\partial y} = \nu\nabla^2\omega + g\alpha\frac{\partial T}{\partial x}, \tag{13}$$

where the vorticity $\omega = \partial v/\partial x - \partial u/\partial y$, and u and v are the velocity components in the x- and y-coordinate directions respectively.

The conduction of heat through either vertical boundary establishes a positive horizontal temperature gradient (with the cold wall to the left, figure 1*a*) which provides the baroclinic generation of positive (i.e. counterclockwise rotation) vorticity at a rate of the order of $g\alpha\partial T/\partial x$. At the same time, the vertical-momentum equation is

$$\frac{\partial v}{\partial t}+\frac{u\,\partial v}{\partial x}+\frac{v\,\partial v}{\partial y} = -\left(\frac{1}{\rho}\right)\frac{\partial p}{\partial y}+\nu\nabla^2 v+g\alpha(T-T_0). \tag{14}$$

At the cold boundary, $u = v = 0$, and $T = T_0 - \Delta T$, and the momentum equation gives (near the wall)

$$\nu \frac{\partial \omega}{\partial x} \sim \left(\frac{1}{\rho}\right) \frac{\partial p}{\partial y} + g\alpha\Delta T. \tag{15}$$

Over most of the vertical boundary the tangential pressure gradient $\partial p / \partial y$ will be very slight. If it is neglected the above equation simply reduces to representing a flux of negative vorticity into the fluid from the boundary due to the relative acceleration between the fluid and the wall caused by the temperature difference. This produces the zero boundary velocity required and counters the positive vorticity baroclinically produced in the near boundary region. The vorticity will then increase from some negative value on the boundary to zero at the point of maximum velocity, and then further increase to a positive maximum before falling away to zero. The zero crossing must be contained in the thermal boundary layer ∂_T, and the vorticity in the region beyond the vorticity maximum is the result of the horizontal diffusion of vorticity by viscosity.

An estimate of the magnitude of the boundary value of vorticity may be obtained by treating the thermal-layer thickness as an estimate for the location of the zero crossing. Initially the thermal-layer thickness grows as $(\kappa t)^{\frac{1}{2}}$, thus

$$\omega_{\text{bdy}} \sim \frac{-Ra\,\kappa^{\frac{3}{2}} t^{\frac{1}{2}}}{h^3}. \tag{16}$$

Initially the vorticity in the interior of the positive maximum peak has been diffused there by viscosity over the evolving viscous boundary layer δ_ν, which scales as $\sigma^{\frac{1}{2}}\delta_T$. An estimate of the peak value may be made, since in this region $\omega \sim \partial v / \partial x$, giving

$$\omega_{\text{int}} \sim \frac{Ra\,\kappa^{\frac{3}{2}} t^{\frac{1}{2}}}{h^3 \sigma^{\frac{1}{2}}}. \tag{17}$$

Similar arguments to those in Patterson & Imberger follow for increasing time. Advection becomes important at times greater than τ, at which time

$$\omega_{\text{bdy}} \sim \frac{-Ra^{\frac{3}{4}}\kappa}{h^2}, \tag{18}$$

$$\omega_{\text{int}} \sim \frac{Ra^{\frac{3}{4}}\kappa}{h^2 \sigma^{\frac{1}{2}}}. \tag{19}$$

Consider now the effect of the horizontal boundary. As the vertical boundary flow approaches the corner, pressure should become important and the flow should experience a deceleration. This will produce vorticity of positive sign at the boundary (Morton 1984), which will act to annihilate the negative vorticity of the flow in the thermal boundary layer. Therefore, we would expect that vorticity would be close to zero at the very bottom (top) of the cold (hot) wall. Eventually the flow is ejected near horizontally by the pressure gradient. The resulting acceleration now generates negative vorticity at the horizontal wall, over a distance approximately equal to that over which vorticity had previously been annihilated.

Positive-vorticity fluid from the viscous boundary layer on the other hand is less influenced by buoyancy. Thus this fluid will be ejected (approximately) radially from the corner. As the pressure gradient driving the flow will be smaller than that for the thermal layer, the ejection rate should be much smaller. The effect is that the positive vorticity collects in the region interior to the thermal boundary layer and the horizontal intrusion, and forms a counterclockwise-rotating region here. A similar mechanism was proposed by Tabaczynski, Hoult & Keck (1970) for flow in a moving corner.

A final source of vorticity production that needs to be considered is the baroclinic production associated with the passage of the initial horizontal temperature intrusions across the cavity. Previously Patterson & Imberger (1980) had only postulated cavity-scale baroclinic vorticity when the intrusion had completely crossed the cavity and was tending to 'pile up' at the opposite side. What is being suggested now is that vorticity will be produced at the head of the intrusion, where temperature gradients are steepest. As the gradients are positive, the vorticity produced would also be positive; however, owing to the smaller temperature gradient, it would be considerably smaller than that adjacent to the hot and cold walls.

4. Numerical resolution

The choice of an appropriate mesh spacing and simulation timestep was in the first instance guided by expectations of the flow based on the scaling results described previously. A satisfactory choice would be one that could adequately resolve the smallest time and lengthscales (see table 1). Implicit in this approach is the assumption that the flow remains laminar. There are good reasons to expect this to be the case. Turner (1973) gives the critical Rayleigh number for the transition to turbulence for the case of convection near a solid, vertical boundary as $Ra \sim 7 \times 10^9$. This is associated with a boundary-layer Reynolds number of a 'few hundred'. Based on the scaled values, our Reynolds number is approximately 80. There is also direct evidence that cavity flows with $Ra \sim O(10^9)$ are not turbulent. The most apt is that from Ivey (1984). The particle track photographs from various stages of the flow all show smooth pathlines, strongly suggestive of laminar flow. Similarly, temperature traces using fast-response thermistors show fluctuations with periods greater than 5 s, seemingly too long for turbulence. Other direct evidence comes from the experiments of Elder (1965). Although those results are for tall narrow cavities, turbulence was seen to commence at Ra greater than $O(10^9)$.

An alternative approach is to use as a guide experimentally observed lengths and times associated with the formation of instabilities prior to the onset of turbulence at higher Rayleigh numbers. When convectively driven flows adjacent to vertical boundaries become unstable, the instability takes the form of a travelling wave disturbance propagating along the boundary layer and at about the same velocity (Gill & Davey 1969). As these instabilities would start to form some distance up the vertical wall where the mesh spacing in the y-direction is relatively large, their scales provide a rational basis for establishing the mesh size to use away from the walls. This approach has the added advantage of being an indirect test of whether turbulence will occur in our problem. If the resolution is sufficient to detect the initial instabilities, and if these are indeed observed, it could be inferred that the flow will become at least partially turbulent. Under these circumstances the model would not be expected to perform well. Elder (1965) has observed such waves, and scaling from his photographs yields a reasonable estimate for the disturbance wavelength as 1.5×10^{-2} m. Assuming that the wave is travelling at the scale velocity of 2.6×10^{-2} ms^{-1}, its period would be 0.6 s.

Tests of mesh spacing were conducted for the two-dimensional 'ideal' case only and

Scale	Value	Eqn	Description
δ_T	1.1×10^{-3} m	(3)	Thermal boundary layer thicknesss
δ_ν	3.0×10^{-3} m	(4)	Viscous boundary layer thickness
τ	9.1 s	(1)	Growth time for thermal boundary layer
V_T	2.6×10^{-2} m s^{-1}	(2)	Velocity in thermal boundary layer
Δ_g	3.5×10^{-3} m	(5)	Inertia buoyancy layer thickness
Δ_ν	Varies with time	(7)	Viscous buoyancy layer thickness
T_ν	1.3×10^{1} s	(6)	Time for viscosity to be important
U_g	6.3×10^{-3} m s^{-1}	(8)	Inertia buoyancy layer velocity
f	1.7×10^{-1} s^{-1}	(10)	Internal wave frequency
T_d	5.7×10^{4} s	(12)	Decay time of internal waves
T_f	1.9×10^{3} s	(9)	Cavity filling time
ω_{bdy}	-1.4×10^{1} s^{-1}	(18)	Negative vorticity generated at sidewall
ω_{int}	5.2 s^{-1}	(19)	Positive vorticity generated by sidewall heating

TABLE 1. Scale values for reference case

used non-uniform meshes of 30 × 30, 40 × 40, 50 × 50, 62 × 62, 74 × 74 and 90 × 90. The number of internal mesh points in each direction is two less than the total number. All mesh spacings used had at least three points within the thermal-boundary-layer scale of the wall (1.1×10^{-3} m) in each direction. Away from the walls the mesh was expanded smoothly, the total points being determined by the degree of spread.

With the exception of the 30 × 30 mesh all produced very similar results. The 30 × 30 mesh failed to adequately resolve the velocity profile along the horizontal boundaries, resulting in the production of 'false vorticity'. Ironically this qualitatively reproduced one of the notable features of Ivey's experiment (the core eddy); however, the predicted velocities in the core were an order-of-magnitude greater than those observed in the experiment.

The 90 × 90 mesh had a maximum spacing of 4.8×10^{-3} m and a minimum spacing of 9.6×10^{-5} m, yielding 7 points within the thermal and 11 points within the viscous boundary-layer scales. The maximum spacing was set according to the instability considerations just noted above. A simulation using this mesh with a 0.25 s timestep was run for 186 s. Figure 2 shows isotherms at the base of the cold wall at $t = 80$ s. There is, as expected, no indication of wave-like instabilities in the vertical boundary layer, confirming the hypothesis that the flow is not turbulent. The slight discontinuities in the isotherms adjacent to the vertical wall are the result of plotter discretization. The vortex region with the distinct temperature inversion near the bottom boundary shows up on all the other simulation meshes used. Results at later times show only very slight differences from the simulations at 50 × 50, 62 × 62 and 74 × 74, which employed 1 s timesteps.

The 50 × 50 mesh had minimum and maximum normalized mesh spacings of 5×10^{-4} and 5×10^{-2} (1.2×10^{-4} and 1.2×10^{-2} m) respectively, and half of the mesh points were within 10 % of the boundary (see the inset to figure 3). Whereas, a timestep of 0.25 s was used with the 90 × 90 mesh, three timesteps were tried with the 50 × 50 mesh: 0.5, 1 and 2 s. The 1 s (actually 1.007 s) timestep gave adequate resolution of the smallest timescales, and restricted the numerical diffusion caused by the backward-Euler timestepping. This scheme has a truncation error with a 'diffusion' coefficient equal to the product of one-half the timestep and the square of the appropriate velocity components. With a timestep of $O(1\text{ s})$, the second derivative in the diffusion term is small where the coefficient is large, so that the

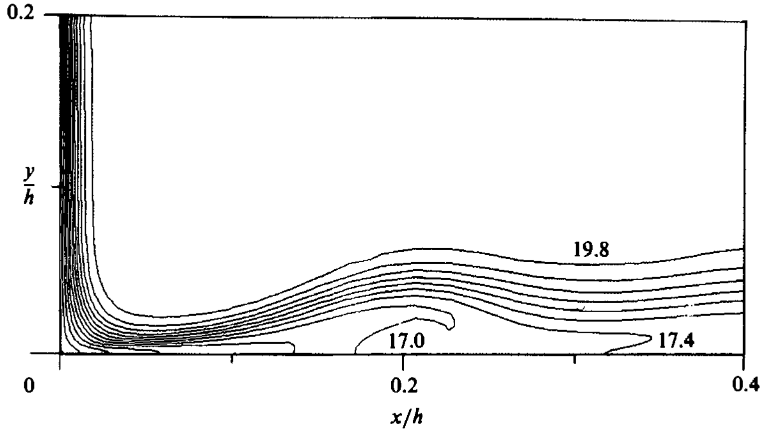

FIGURE 2. Temperature contours at base of cold wall at $t = 80$ s for 90×90 simulation. Values shown are in °C. Contour increments are 0.4 °C.

diffusion terms are small compared with other terms. Elsewhere the 'diffusion' coefficient is generally significantly smaller than the kinematic viscosity or the thermal diffusivity and so its effects are negligible. When a timestep of 2 s was used some of the fine structure was lost, although the global flow pattern was almost identical. The 0.5 s timestep result was indistinguishable from the 1 s result. As seen in figure 3 the 50×50 and 90×90 meshes give equivalent results and the former was adopted for production runs.

Unless otherwise noted, the results presented are from the 50×50 mesh in conjunction with a 1 s timestep. The code was run on the CRAY X/MP at the San Diego Supercomputer Center. CPU time for the two-dimensional 'ideal' case was 4900 s for 2500 s of simulation. (Longer timesteps, with a subsequent reduction in run time, could probably have been employed after 800 s with little loss of accuracy.)

5. Simulation results

The results presented are those for the reference case and four variations to the conditions assumed for this case. The adoption of the two-dimensional case as the reference was motivated primarily by the need to minimize computer usage, while at the same time capturing the essential physics of the problem. It is probable that there will be some difference between the two-dimensional simulation and the three-dimensional experiments, particularly in the latter stages of the flow. Indeed, while the width and depth of Ivey's apparatus were 0.24 m, its span was 0.2 m, yielding a spanwise aspect ratio (span/height) of 0.83. In similar size apparatus, Koseff & Street (1984) found significant influence from endwalls for a lid-driven flow. In the fully developed state the measured flow in the vertical plane was weaker than that calculated by accurate two-dimensional simulations although the primary flow features were similar. In comparison, three-dimensional simulations of the flow by Freitas *et al.* (1985) show quantitative agreement with the experimental results. Mallinson & de Vahl Davis (1977) also showed that the predominant vertical-plane features of flows similar to those considered here remained qualitatively the same in two and three dimensions. The differences that arise concern only the weakening of the flow and the longer approach to steady state for the two-dimensional simulations (owing to the absence of viscous drag from the endwalls and the creation of secondary flow structures in the spanwise planes). Thus, a two-dimensional simulation can be used to understand the essential physics. This is particularly so in our case where we are primarily concerned with the behaviour in the very early stages of transient flow.

5.1. *Reference case*

The reference-case flow occurs in a square cavity of dimension 0.24 m, with rigid, non-slip boundaries and containing water at rest and at temperature $T_0 = 20$ °C. The upper and lower boundaries are perfectly insulated. At time $t = 0$, the right and left sidewalls are instantaneously heated and cooled to T_0+5 °C and T_0-5 °C, respectively, and thereafter maintained at these temperatures. This flow has the same spatial dimensions and the same nominal temperature difference between the vertical boundaries as used by Ivey (1984) The total time simulated was 2500 s.

As expected, boundary layers form adjacent to the hot and cold walls. It takes approximately 10–20 s for these to reach a quasi-steady state, in good agreement with the scale time of 9.1 s. Figure 3 presents profiles of temperature, vertical velocity and vorticity immediately adjacent to the midpoint of the cold boundary at 20 s for the 50×50 simulation. The scaled thicknesses of the thermal and viscous boundary layers are also indicated. These appear to be underestimates, and as a result the scaled velocity is larger than the simulated result. The vorticity profile accords with the description advanced in the previous section, although the scaling overestimates the values of the vorticity peaks. The temperature and velocity profiles for the 90×90 calculation are also shown on figure 3. The difference between the velocity peaks of the two simulations is less than 5%. The symbols indicate the location of mesh points.

A series of pathline plots (beginning with figure 4*a*) is used to illustrate the complex and rapidly changing features of the transient flow. The pathlines are the traces of 'particles' initially positioned at every fourth mesh point and subsequently moved with the calculated velocities at the end of each 1 s timestep. The dots on the figures are the particle positions at the beginning of the 10 s timespan indicated. The traces are analogous to flow visualization using neutrally buoyant particles in a laboratory experiment and so allow comparison with Ivey's results. Note, however, that Ivey used 15 s photographic exposures. Temperature contours at the end of each of the time spans are also presented (beginning with figure 4*b*). The maximum and minimum contour values shown are 24.6 °C and 15.4 °C and the interval between contours is 0.4 °C. The insets in each of the temperature contour plots show an enlarged view of the bottom of the cold wall.

In figure 4(*a*) the vertical-wall flow is clearly evident. The flow emerging at the top of the hot wall and the bottom of the cold wall (the emergent corners) appears generally to have two parts – a horizontal intrusion and a potential flow. The temperature contours in figure 4(*b*) show the commencement of the horizontal intrusions. The warm (upper) intrusion is advancing slightly faster than the cool (lower) intrusion, owing mainly to the lower viscosity and high coefficient of thermal expansion of the warm water. The 6 mm thickness of these intrusions agrees well with the scale thickness of 4 mm.

During the next 10 s, eddies at the top and bottom emergent corners become more pronounced, as shown in figures 4(*c*, *d*). The beginnings of separation zones at $x/h = 0.87$ on the upper boundary and $x/h = 0.13$ on the lower boundary are also discernible. Between these two flow features the intrusions themselves appear to be in transition. Rather than continuing to propagate as thin layers along the

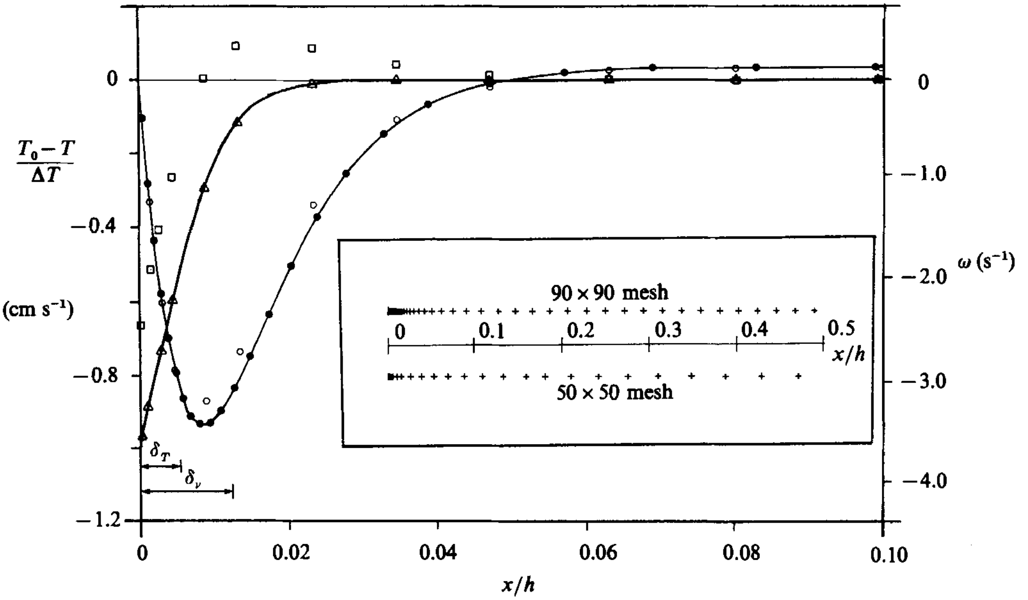

FIGURE 3. Profiles of temperature (△), vertical velocity (●, ○) and vorticity (□) (for 50 × 50) normal to the midpoint of the cold boundary at $t = 20$ s. Symbols show the location of mesh points. Profiles from the 90 × 90 simulations are shown in full line (with symbols superimposed on velocity profile), while profiles from the 50 × 50 simulation are shown in symbols only. The thicknesses of the thermal and viscous boundary layers based on the scaling analysis are indicated. Inset: schematic of the mesh spacing used in the 90 × 90 and 50 × 50 simulations. The meshes are symmetric about the centreline ($x/h = 0.5$) and identical in both the x- and y-directions.

boundaries, they have rapidly widened to ~ 20 mm, a value 6 times larger than the scale thickness suggested by (7). The reasons for such a transition are unclear. One possibility is simply that the corner eddies are sufficiently strong to entrain part of the intrusion, causing the emergent flow to diverge. The adverse pressure gradient produced by such a flow would also account for the formation of the separation zones.

Ivey (1984) suggested that similar experimentally observed features could be internal hydraulic jumps. Defining the Froude number of the emergent flow as $F = u/[g(\Delta\rho/\rho)\Delta]$, where u and $\Delta\rho$ are a characteristic velocity and a density difference at the narrowest width, Δ, of the emergent flow, we estimate Froude numbers in the range 0.7–1.5, thus making this explanation plausible. For Froude numbers less than 1.7, hydraulic jumps are undular (Henderson 1966) and take the form of smooth standing waves with small energy losses. The present simulation is a full or direct simulation and while no account is taken of turbulent features of breaking phenomena associated with a usual hydraulic jump, the simulation should adequately represent an undular jump.

An alternative explanation is that the intrusion is forced to flow under (over) undisplaced, relatively cool (warm) fluid on the top (bottom) of the cavity. This explanation agrees with the occurrence of temperature reversals in the intrusions (see for example, figure 4*d*). A related experiment by Worster & Leitch (1985) showed a similar phenomenon. They accounted for the separation zone as an inertial affect associated with rebound of the emergent flow.

Over the next 30 s the area of influence of the eddies continues to grow, and they

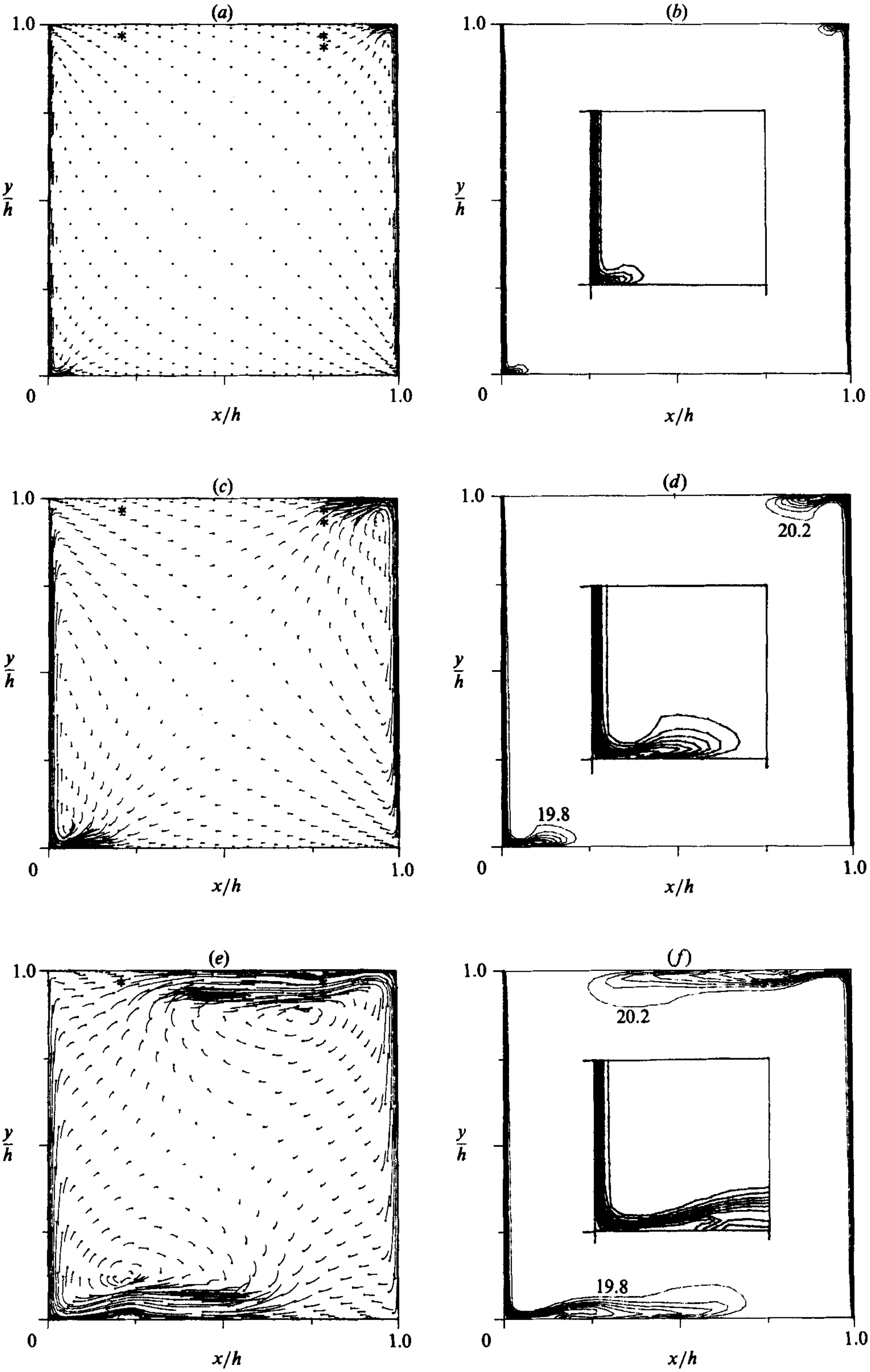

FIGURE 4(a–f). For caption see page 134.

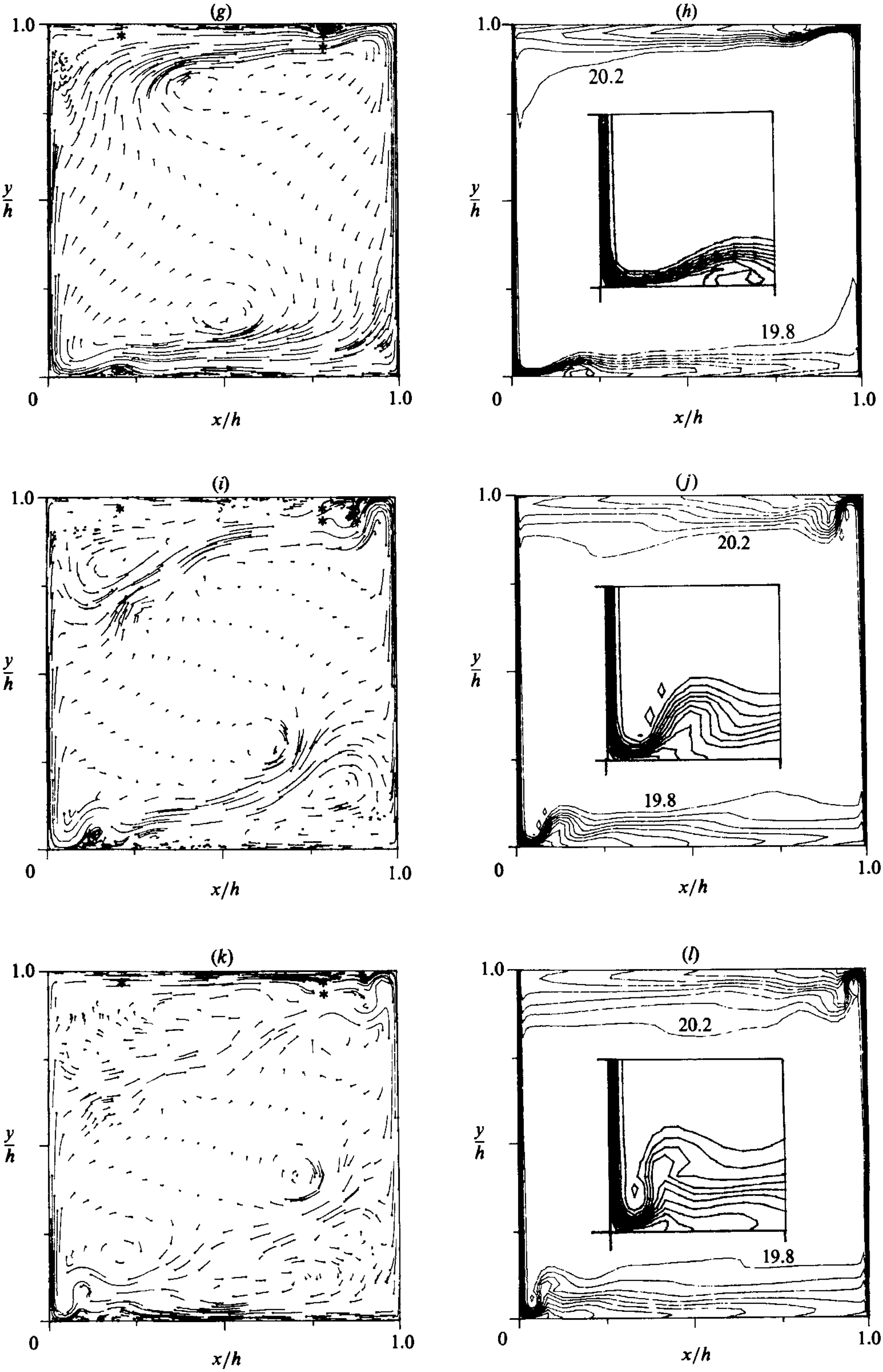

FIGURE 4(*g*–*l*). For caption see page 134.

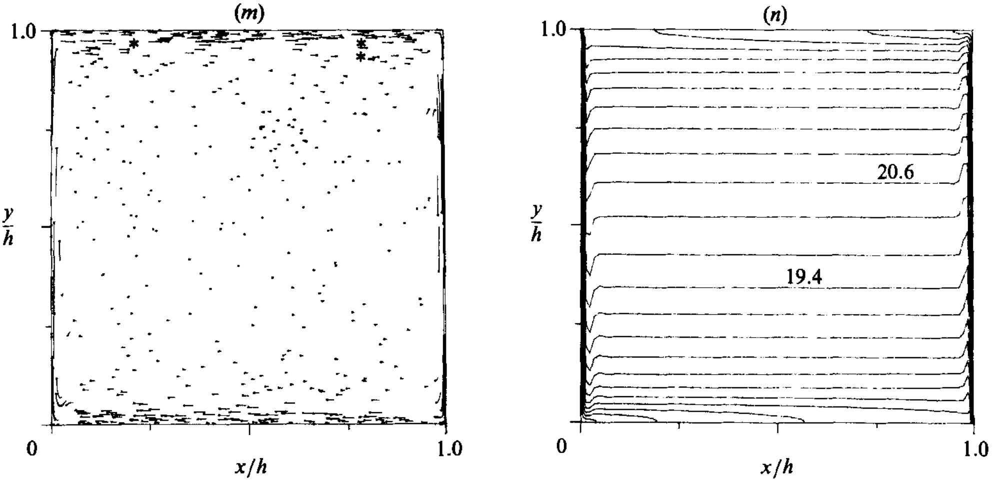

Figure 4. Evolution of transient flow for two-dimensional cavity simulation. Pathlines are for the time intervals (*a*) 0–10 s; (*c*) 10–20 s; (*e*) 40–50 s; (*g*) 80–90 s; (*i*) 120–130 s; (*k*) 160–170 s; (*m*) 1900–2000 s. Temperature contours are for (*b*) 10 s; (*d*) 20 s; (*f*) 50 s; (*h*) 90 s; (*j*) 130 s; (*l*) 170 s; (*n*) 2000 s. Left wall is at 15 °C and right wall is at 25 °C. Values shown are in °C. Isotherms are at 0.4 °C intervals. Asterisks in (*a*), (*c*), (*e*), (*g*), (*i*), (*k*) and (*m*) show locations of temperature probes (see Figure 1*a*). Inset on temperature contour plots extends from the origin to $x/h = 0.26$ and $y/h = 0.2$.

appear to move away from the vertical walls as shown in figure 4(*e*). This is not so much the result of advection of an existing vortex, but rather the result of the baroclinic generation of fresh vorticity by the advancing thermal front. The intrusions are now almost two-thirds of the way across the cavity with their thickness being relatively stable at about 20 mm (figure 4*f*). Note the temperature reversals adjacent to the horizontal boundaries in each of the intrusions. The flow in the isothermal core is dominated by the eddies and by entrainment into the vertical boundary flows. This produces a net effect of a weak downflow on the side closest to the cool wall and upflow on the opposite side.

By time $t = 80$ s, both intrusions have crossed the cavity as evidenced by figure 4(*g*, *h*). The isotherms clearly show a 'piling up' of the temperature-affected fluid at the ends of the intrusions, suggesting that seiches are possible. In fact this process has already commenced for the case of the hot intrusion as shown by the sharp turn in the pathlines in the top left-hand corner. The same process commences in the opposite corner seconds later. Also noticeable are the distinct circulations in the separation zones.

The flow reversal in the upper-left and lower-right corners caused by the internal waves is graphically illustrated in figure 4(*i*) for time interval 120–130 s. The flow along the top and bottom boundaries has been greatly reduced and at times even reversed owing to the passage of the wave. In figure 4(*j*) the slope of the isotherms in these regions is also clearly reversed. The separation zones have been squeezed by the flow and forced back towards their respective emergent corners, suggesting that the internal wave effect is indeed cavity wide. The very complicated temperature structure around the separation zones and the temperature inversions referred to previously ensure that the wave description will not be simple. The core is still essentially isothermal and so internal wave effects are confined to the intrusion zones only. Core velocities are still low and flow direction is predominantly as before. The eddies now appear to be centred on the opposite side of the cavity. They are commencing to lose their identities as their vorticity diffuses and production is reduced with the weakening of the horizontal temperature gradients. The anomolous blobs of warmer and colder fluid in the lower and upper emergent corners are the result of slight overshoots and undershoots produced by the quadratic upstream differencing of the convected quantities (McGuirk, Taylor & Whitelaw 1982). These occur where sharp gradients exist sufficiently far from the areas of high grid packing at the walls. Tests with different mesh refinements (a finer mesh producing a smaller over/undershoot) confirm that with the 50 × 50 mesh the features have no significant influence on the dynamics of the flow.

By time interval 160–170 s (figure 4*k*, *l*) the internal waves are clearly moving in the opposite direction to the previous time interval. The intrusion velocities are however clearly lower than they were at earlier stages in the flow. As the strongly stratified regions start to occupy a larger part of the cavity there is definite detraining of fluid from the vertical boundary layer at points other than the emergent corners. This would appear to match the observations of Worster & Leitch (1985).

At the time interval 1900–2000 s, the flow is nearing its steady-state condition. In figure 4(*m*) the pathlines show that the velocities in the core are almost completely horizontal, with maxima occurring near the top and bottom boundaries and zero velocity near midheight. In the upper half of the cavity the flow is exclusively to the left and in the lower half, to the right. These flows support the entrainment from the lower (upper) half of the hot (cold) wall and the detrainment from the upper (lower) half. The fact that the detraining flows are now carried by the entire cavity depth rather than by two thin intrusion layers accounts for the lower overall velocities evident in the figure. Clearly visible is the vertical flow reversal at the detraining portion of the vertical boundaries (Gill 1966). The temperature contours in figure 4(*n*) show the entire cavity to be vertically stratified at this time. The gradient is weakest at midheight; however it continues to strengthen with time.

A comparison between the flow fields generated by the 50 × 50 mesh and the 90 × 90 mesh is afforded by the velocity-vector plots at $t = 80$ s shown in figure 5(*a*, *b*). The vectors in each have been plotted at the same scale. The two fields are very similar, the most pronounced differences being the ability of the finer mesh to provide slightly sharper definition of the recirculation zones on the horizontal boundaries, and to resolve two very weak eddies adjacent to each of the intrusions. For the latter, the coarser grid produced a single, weak eddy adjacent to the intrusions.

The description of the flow advanced on the basis of vorticity considerations can also be confirmed by viewing contours of vorticity. Figures 6(*a*, *b*) shows vorticity contours at the top of the hot wall at two times. The values of the vorticity contours range from $0.2\ \mathrm{s}^{-1}$ (the innermost contour on both) to $-2.6\ \mathrm{s}^{-1}$ at 10 s and $-3.8\ \mathrm{s}^{-1}$ at 20 s. Immediately adjacent to the vertical wall, negative vorticity diffuses away from the generation site at the wall. Sufficiently far from the wall, vertical advection dominates, hence the relatively broad region of high ($> 0.2\ \mathrm{s}^{-1}$) positive vorticity. In the vertical direction the negative vorticity is seen to diminish only when the flow is within the top 5% of the wall, and to approach zero at the corner. Regeneration of negative vorticity occurs over an equally short distance along the top wall. These regions correspond to areas of high tangential pressure gradient.

As suggested previously, the advected positive vorticity in figures 6(*a*, *b*) tends to accumulate near the emergent corners. Figure 7(*a*, *b*) shows only the positive vorticity at 20 and 50 s for the full cavity. Contour intervals are at $0.02\ \mathrm{s}^{-1}$. What is

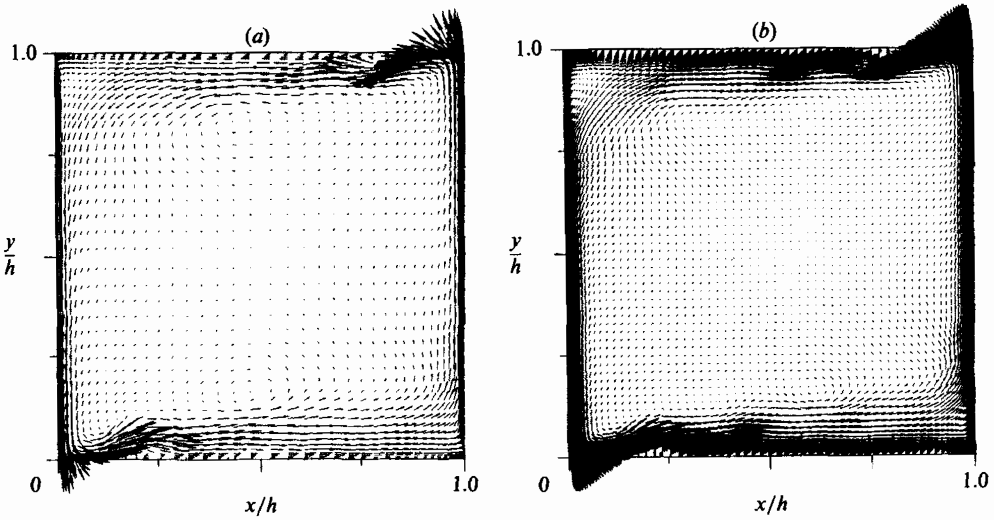

FIGURE 5. Velocity vector plot at $t = 80$ s for (a) 50×50 simulation, and (b) 90×90 simulation.

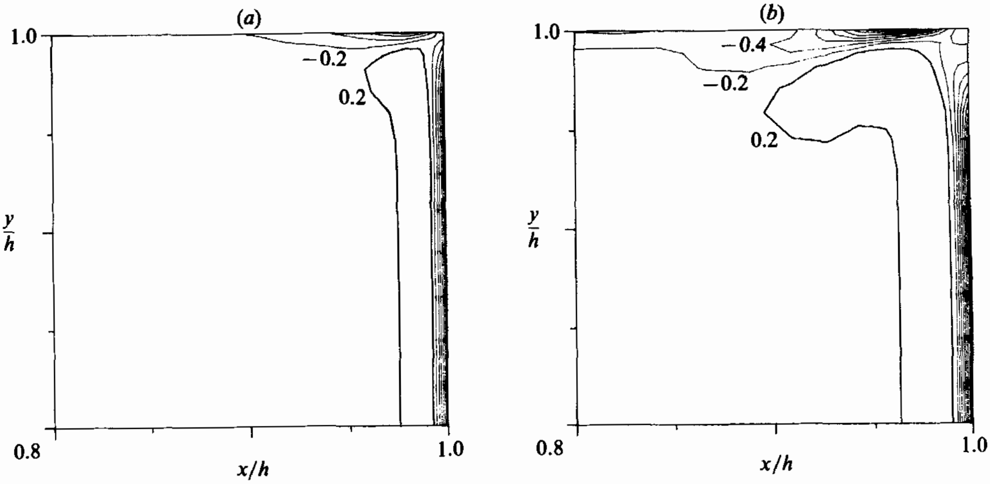

FIGURE 6. Vorticity contours in upper right-hand corner of two-dimensional cavity at (a) 10 s and (b) 20 s. Positive vorticity contours are shown as bold lines. Values shown are in s^{-1}. Contour interval is $0.4\ s^{-1}$.

now evident, with the lower vorticity contours, is the existence of the secondary region of positive vorticity generation associated with the head of the intrusion. Thus, what appeared in figure 4(e) to be a single eddy just below the upper intrusion, has in fact two 'vorticity centres'.

The pathline photographs from Ivey (1984) have much in common with the flow described above. For example, structures that appear very similar to the flow separations and depth transitions above appear in the photographs at approximately the same locations. However, the core flow is radically different. The simulation shows core motions that are controlled by entrainment to the vertical boundary layers and the influence of the two positive vorticity regions generated by the advancing intrusions. The experiment by comparison shows a core that, from

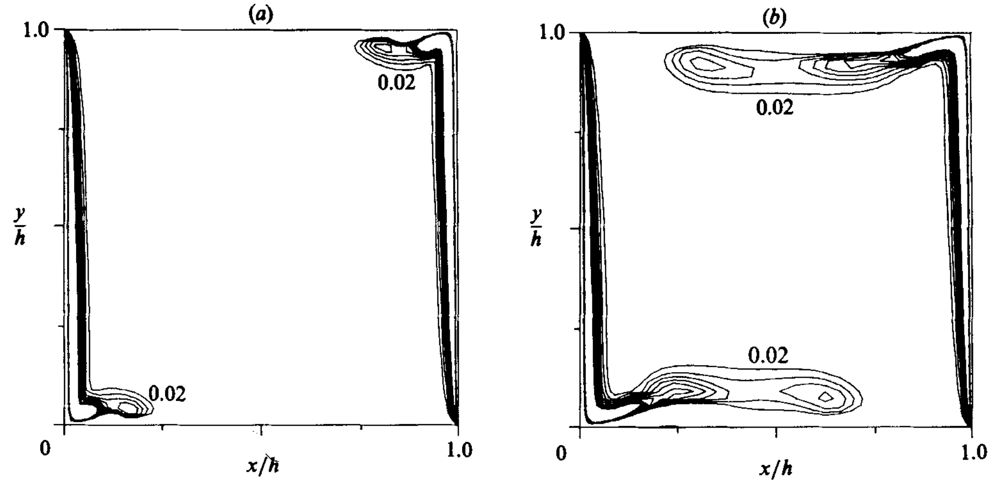

FIGURE 7. Positive vorticity contours for two-dimensional cavity at (*a*) 20 s and (*b*) 50 s. Values shown are in s^{-1}. Maximum contour value is $0.2\,s^{-1}$. Contour interval is $0.02\,s^{-1}$.

approximately 80–130 s, is dominated by a single, central vortex of negative vorticity. The mere existence of negative vorticity in the core is difficult to reconcile with the description of vorticity generation presented above. We return to this point later.

Data from thermistors at three points in the warm intrusion led Ivey to conclude that oscillations in the transient flow existed, but that they did not extend across the full width as would a seiche. In the simulated flow seiches are present, as already demonstrated by the pathlines and the temperature contours. This difference between the numerical and the experimental results can be accounted for quite simply, however. The asterisks in the pathline plots show the locations of the thermistors (also see figure 1*a*). It is evident that the two on the right are very close to the separation zone for much of the time. Changes in point temperatures associated with the observed migration of this zone are far greater than those attributable to the seiche, and so the temperature response at opposite sides of the cavity will be very different and largely uncorrelated. Furthermore, as the left-hand thermistor is at about the level of the temperature reversal noted earlier, oscillations at that point would appear quite weak. A point lower down in the intrusion would see a more pronounced variation in temperature.

Figure 8(*a*) presents non-dimensionalized temperature traces from the simulation for the same points, overlaid by Ivey's experimental data. The dashed lines represent experimental data for the case where $\Delta T = 4.8\,^{\circ}C$ and $\sigma = 7.1$, while the dotted lines are for $\Delta T = 5.0\,^{\circ}C$ and $\sigma = 6.6$. (Note that the Rayleigh number as we define it is a factor of two larger than that of Ivey.) These deviations from the simulation conditions should produce only a small change. However, the agreement between the numerical and the experimental results is poor. The temperature differences produced in the simulation are as much as a factor of two greater than those observed in the experiments and rise at much faster rate. The time at which a temperature rise is initiated is also slightly larger in the experiment. These points of difference will be considered further in the discussion of the results from variations to the reference case.

The weak oscillation at point 3 noticeable in both the simulated and the

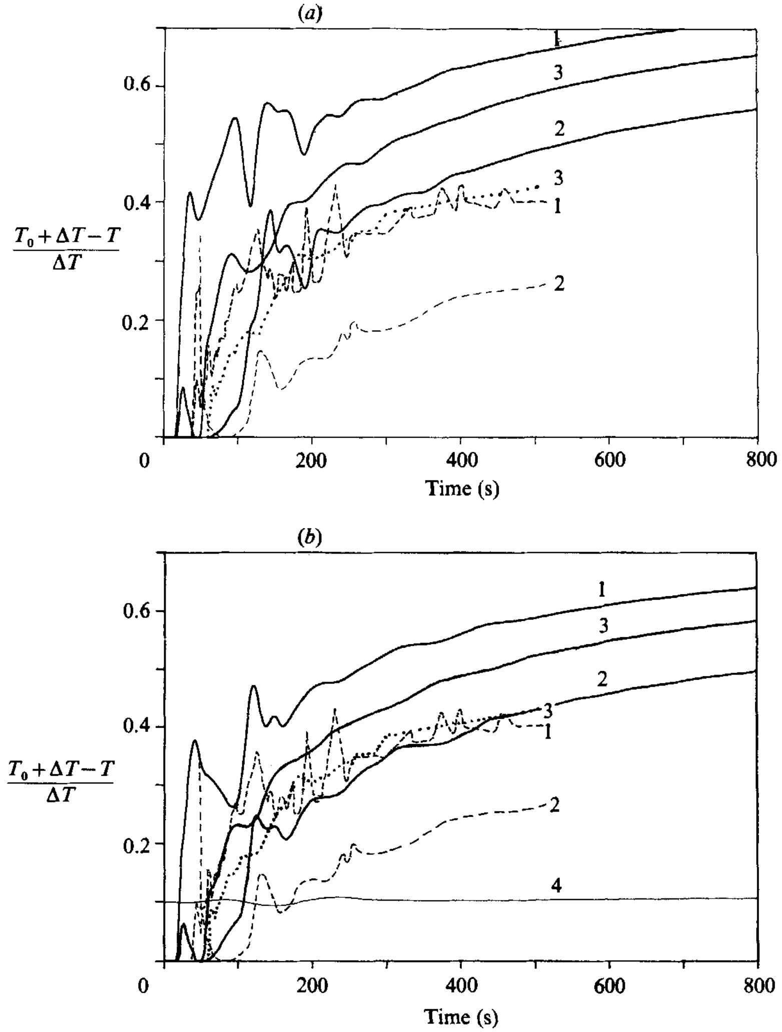

FIGURE 8. (*a*) Traces of non-dimensionalized temperature from points 1, 2 and 3 (see figure 1) for initially homogeneous cavity ($\Delta T = 5.0$ °C and $\sigma = 7.1$). Traces from experiments are overlayed as dashed lines ($\Delta T = 4.8$ °C and $\sigma = 7.1$), and dotted lines ($\Delta T = 5$ °C and $\sigma = 6.6$). (*b*) Traces on non-dimensionalized temperature from points 1, 2, 3 and 4 (see figure 1*a*) for initially stratified cavity. The trace for point 4 has been offset vertically by 0.1 for clarity.

experimental result. This is the only evidence of a seiche that the instrumentation could provide. Its period is 60–70 s, which compares favourably with the 40 s suggested by the scaling.

The clearest demonstration that a seiche is generated when the intrusion reaches the opposite side of the cavity is a plot of Nusselt number against time. The Nusselt number was evaluated at the hot and cold vertical boundaries and at the centreline between these two boundaries by vertically integrating the equations

$$Nu_{\mathrm{bdy}} = \frac{K\left(\dfrac{\partial T}{\partial x}\right)}{\bar{K}\left(\dfrac{2\Delta T}{h}\right)}, \tag{20}$$

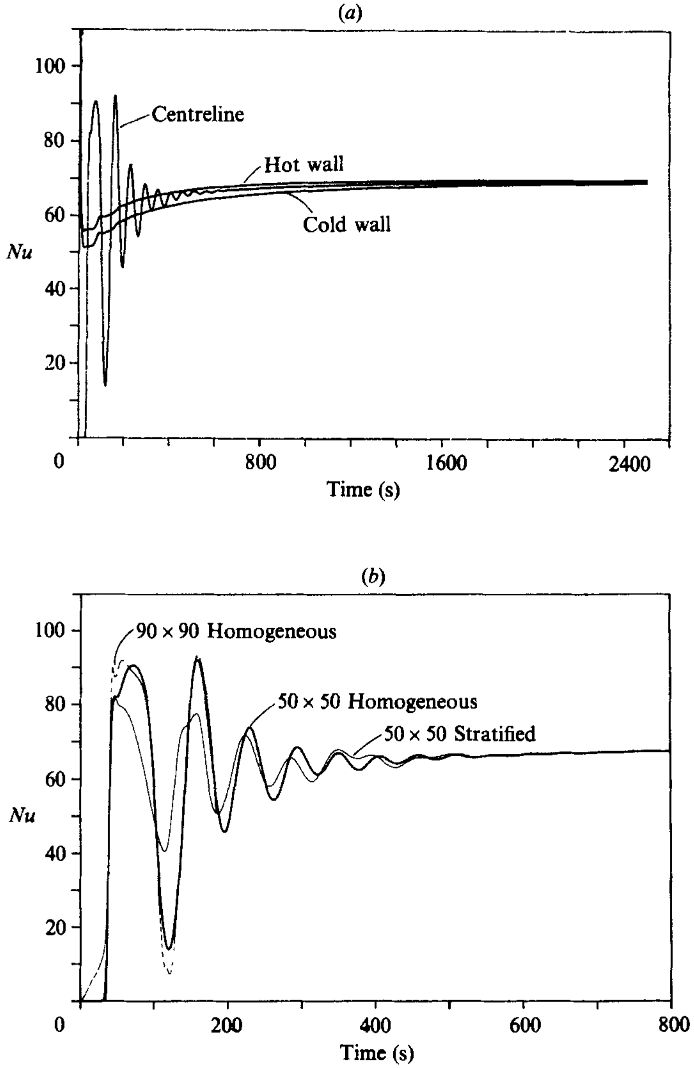

FIGURE 9. (*a*) Nusselt number at the hot wall, the cold wall and the centreline as a function of time for 50 × 50 simulation. (*b*) Comparison of the centreline Nusselt number for the 50 × 50 simulation, the 90 × 90 simulation and the 50 × 50 simulation with 0.5 °C vertical temperature difference.

and

$$Nu_{\text{cen}} = \frac{\left[K\left(\dfrac{\partial T}{\partial x}\right) - C_p\,\rho T u\right]}{\bar{K}\left(\dfrac{2\Delta T}{h}\right)}, \tag{21}$$

where K is the thermal conductivity, C_p is the specific heat at constant pressure, and the overbar indicates an average over the whole cavity. Figure 9 (*a*) shows the result. The Nusselt number at the centreline can clearly be seen to be oscillatory, a reflection of the strongly fluctuating velocity associated with a seiche. The oscillations were damped after about 600 s, two orders-of-magnitude sooner than suggested by the scaling. The fact that the scaling employed by Patterson & Imberger (1980) was a simple momentum/diffusion timescale based on the cavity height h accounts for this.

As the internal waves are confined to the region of the intrusions, a more appropriate lengthscale would be one that relates to the thickness of the intrusion. (This would also produce a better estimate for the internal wave period.) As noted above, the present scaling of the intrusion thickness is itself questionable. However, based on the observation that the intrusion thickness is approximately one-tenth the cavity dimension by the time it has traversed the cavity (see figure 4*h*, *j*), a better first estimate of the decay time of the internal wave would be $(0.1\,h)^2/\nu \sim 570$ s, in good agreement with the simulated value.

Attainment of steady state would coincide with all three Nusselt numbers collapsing to a single, constant value, a condition that the simulation is obviously approaching. The difference between the Nusselt numbers at the hot and cold walls is a result of the temperature dependence of the fluid properties. They cause the thermal boundary layer at the hot wall to be thinner than that at the cold wall. Thus the Nusselt-number difference will disappear only when the temperature in the core rises enough above 20 °C to compensate by increasing $\partial T/\partial x$ at the cold wall relative to that at the hot wall. The Nusselt number across just the centre of the cavity for both the 50×50 and 90×90 simulations is shown in figure 9(*b*). The difference can be seen to be very small for the 186 s simulated.

5.2. *Variations from the reference case*

5.2.1. *Gradually heated sidewalls*

As a temperature difference cannot be generated instantaneously in a physical experiment, an attempt was made to simulate this condition numerically. In this case the temperature boundary condition on the hot and cold walls was ramped linearly from T_0 at $t = 0$ to $T_0 \pm \Delta T$ at $t = 5$ s. Five seconds was the time required for Ivey's experiment to produce a constant temperature difference across the cavity. The effect on the simulated flow field and temperature contours was negligible over the 200 s calculated.

5.2.2. *Non-insulated upper and lower boundaries*

Non-insulated upper and lower boundaries are likely to exist in physical experiments. In this case, the conditions were suggested by the uninsulated bottom boundary of Ivey's cavity. In fact a more extreme case was simulated, specifically both the upper and lower boundaries being maintained at the ambient temperature of 20 °C. The results for a 200 s simulation, however, showed that the effect on the transient flow was insignificant and pathline plots were virtually identical to those of the reference case. The heat flux in the intrusions is so strongly controlled by advection during the early stages of the flow that the conductive effects are negligible. Such a result was predicted by Gill (1966).

5.2.3. *Three-dimensional cavity*

A three-dimensional simulation was conducted while treating the centreplane in the spanwise direction as a symmetry plane. The endwall was assumed to be insulated. This use of the half-cavity greatly reduces CPU time and storage requirements compared with the full three-dimensional simulation. Test runs showed no difference between simulations for a half-cavity and a whole cavity. A $50 \times 50 \times 19$ mesh was used for the half-cavity simulation. The horizontal span of the half-cavity was 0.1 m, making the geometry identical to that of the experimental facility used by Ivey. The simulation was terminated at 800 s.

Velocity-vector plots in particular planes are used to illustrate the resulting flow

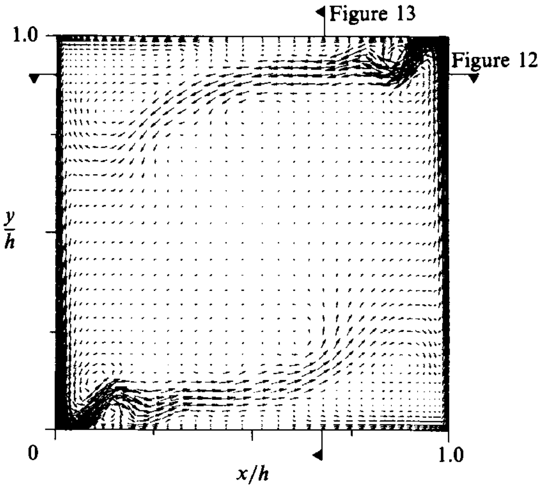

FIGURE 10. Velocity vectors at 120 s on the vertical (x, y)-plane at $z/W = 0.5$, for three-dimensional simulation (see figure 1*b*).

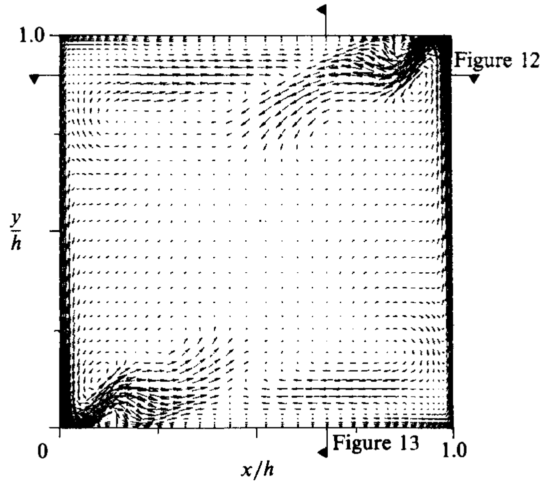

FIGURE 11. Velocity vectors at 120 s on the vertical (x, y)-plane at $z/W = 0.045$, for three-dimensional simulation.

(see figure 1*b*). Figure 10 is a plot on the centre (x, y)-plane $(z/W = 0.5)$ at time $t = 120$ s; W is the full cavity span. It is clear that there is little difference betweeen this flow and the two-dimensional flow in figure 4(*i*). The corresponding temperature contours (not shown) also are in good agreement. Therefore, at this point of time in the solution, on the centreplane there was little apparent difference between the two- and three-dimensional simulated flows, and certainly nothing to account for the core vortex observed in the experiments.

Away from the centreplane the flow is strongly influenced by three-dimensional effects. Figure 11 shows a velocity-vector plot in the vertical (x, y)-plane at $z/W = 0.045$. The flow is clearly different from that at the centreplane, with reversing flows actually ocurring within both intrusion layers. However, the flow direction in the core is still largely controlled by entrainment into the vertical boundary layers and so still differs from the experimental observation. A better picture of the nature

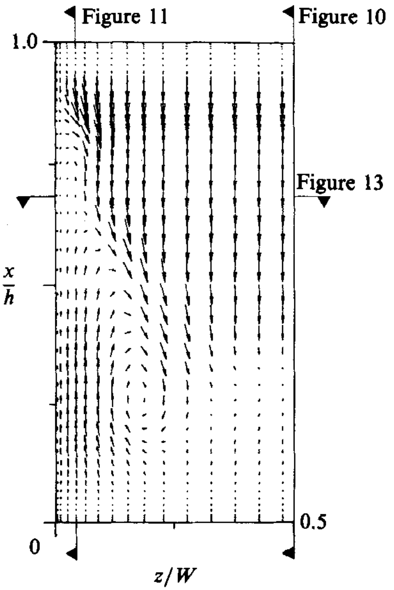

FIGURE 12. Velocity vectors at 120 s on the horizontal (x, z)-plane at $y/h = 0.9$, for three-dimensional simulation.

of these reverse flows is gained by viewing velocity vectors in the horizontal (x, z)-plane. In figure 12 the plane at $y/h = 0.9$ clearly shows the endwall exerting a very large effect on the flow field. At this level the flow shown is within the temperature-stratified intrusion layer. Interestingly some of the largest velocities are away from the centreplane.

Views of the velocity vectors in the vertical (y, z)-plane (parallel to the hot and cold walls) show other surprising flow patterns. In figure 13 a section at $x/h = 0.68$ reveals vortices in the region below the temperature stratification. These structures appear to exist in the upper half of the cavity on the side closer to the hot wall and in the lower half of the cavity on the side closer to the cold wall.

Temperature traces at points on the centreplane coinciding with Ivey's measurement points produce very similar results to the two-dimensional result shown in figure 8(*a*). The differences between the simulated traces and the experimental traces described previously still remain. Nusselt numbers were calculated at the walls and across the centreline. Rather than integrating across the full cavity depth (in the z-direction) they were calculated over strips defined by the mesh points in the z-direction. Values for Nusselt number at the hot and cold walls at all values of z/W were virtually unchanged from the two-dimensional result. Nusselt numbers across the centreline, however, did vary with z/W. These differences were in both the amplitude of the oscillations and in their phase. However, they did not manifest themselves near the symmetry plane until after almost 300 s, well after the time of influence of the core eddy. Thus three-dimensional effects appear to play no role in the formation of the core eddy. (Details of this three-dimensional flow will be presented in a separate contribution.)

5.2.4. *Initially stratified ambient*

As a final variation from the ideal case, a stable stratification with a linear, vertical temperature distribution was imposed on the two-dimensional cavity as an initial condition. Four temperature gradients were simulated. These were 4.17, 2.08, 1.25

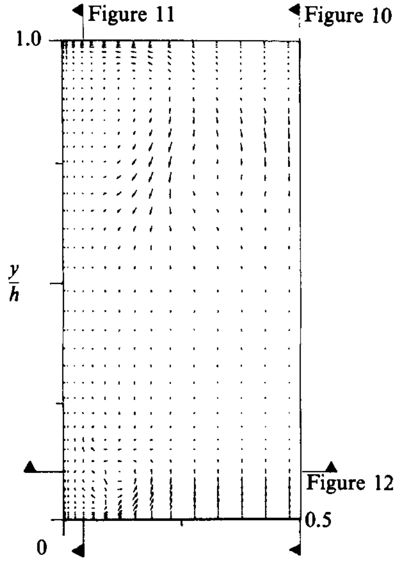

FIGURE 13. Velocity vectors at 120 s on the vertical (y, z)-plane at $x/h = 0.68$, for three-dimensional simulation.

and 0.42 °C m^{-1}, corresponding to vertical temperature differences from top to bottom of 1.0, 0.5, 0.3 and 0.1 °C respectively. Qualitatively the results for all four cases were similar, and the quantitative differences were small. Accordingly, only the results for the 0.5 °C difference are presented. (G. N. Ivey (personal communication, 1988) considers 0.5 °C an upper bound of possible difference.) Figure 14 shows a sequence of 10 s pathlines for four time intervals. From the time the intrusions start to propagate across the cavity the distinction in the two flows is apparent. In figure 14(*a*) (40–50 s) it is clear that the production of the core eddies, previously located adjacent to the intrusions in figure 4(*e*), is being suppressed. In figure 14(*c*), 20 s later, the flow direction in the upper-left and lower-right areas of the core has been turned by almost 90° from the previous figure, in a further departure from the unstratified case. But, it is only in figure 14(*e*) that the radical difference in the flow pattern becomes apparent. For the time interval 80–90 s the core is seen to be dominated by a large, elongated, single vortex which is tending to move fluid up the cold side and down the warm side. Thus, the state that could not be realized in the reference case, i.e. the core dominated by negative vorticity, does in fact occur when the cavity is stratified. The agreement between this figure and Ivey's (1984) figures 2(*b*) and (*g*) is remarkable. The flow in the top intrusion has also commenced reversing itself, again suggesting the presence of internal waves within the intrusions. Twenty seconds later, in figure 14(*g*), the vortex can be seen to be even more pronounced. This agrees with Ivey's figure 2(*c*), where a distinct lengthening of the streaks is apparent. As time continues the core vortex slows and reverses direction, after which time the approach toward steady state is not unlike that taken by the unstratified cavity.

The reason for the generation of this flow pattern becomes clear when the temperature contours are examined. At $t = 40$ s (figure 14*b*) the 20 °C isotherm across the centre of the core is essentially horizontal. By $t = 60$ s (figure 14*d*) it has started to tilt, partially in response to the entraining flow into the vertical boundary layers and partially in response to the influence of the intrusions. This

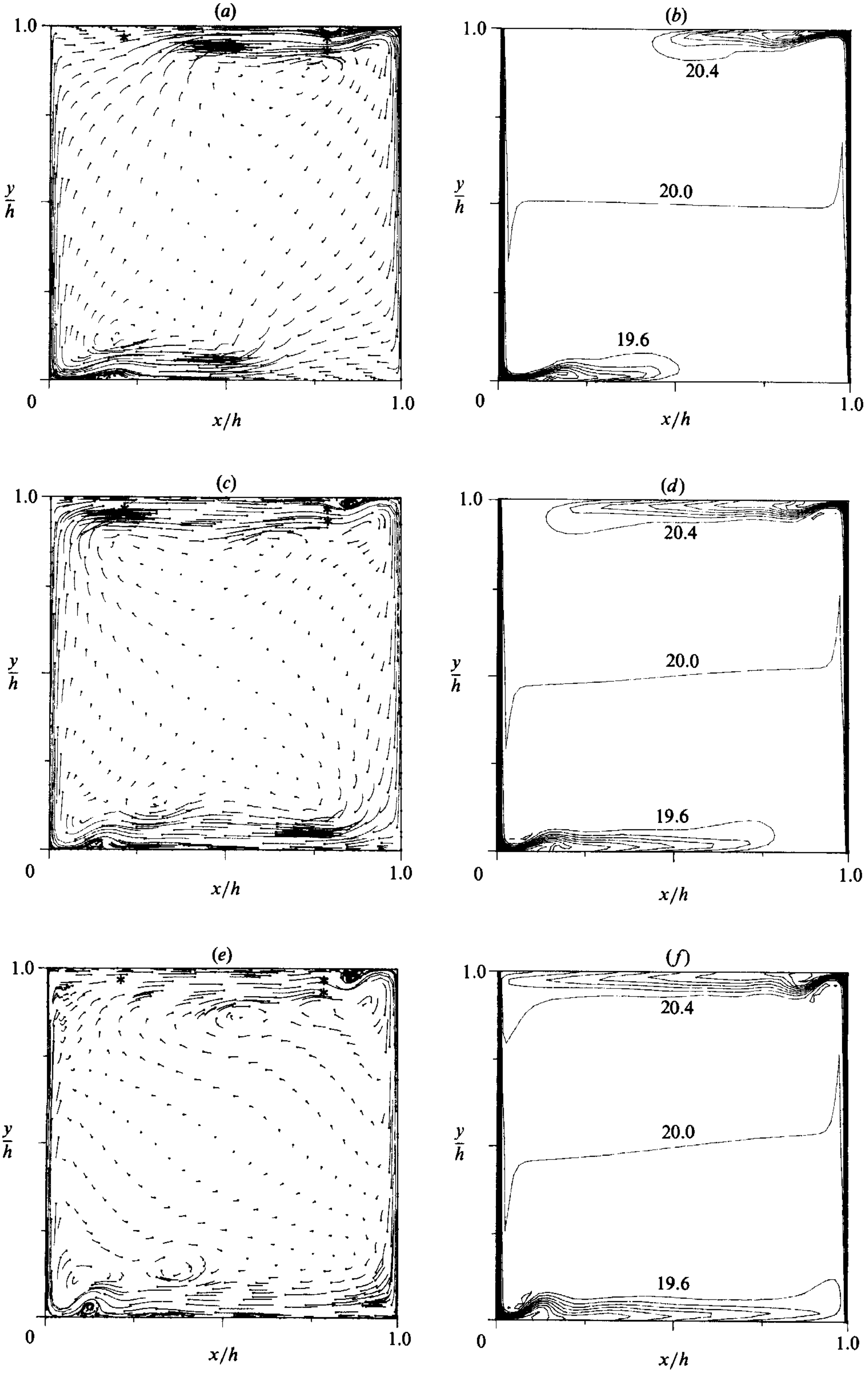

FIGURE 14(*a–f*). For caption see facing page.

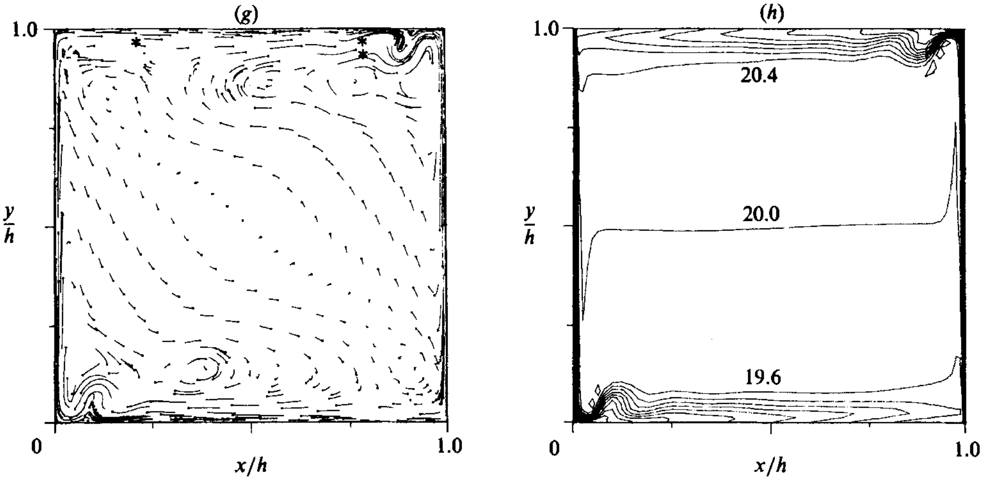

FIGURE 14. Pathlines and temperature contours for two-dimensional cavity simulation with 0.5 °C vertical temperature difference. Pathlines are for the time intervals (*a*) 40–50 s; (*c*) 60–70 s; (*e*) 80–90 s; (*g*) 100–110 s. Temperature contours are for (*b*) 40 s; (*d*) 60 s; (*f*) 80 s; (*h*) 100 s. Left wall is at 15 °C and right wall is at 25 °C. Values shown are in °C. Isotherms are at 0.4 °C intervals.

tilting is continued at $t = 80$ s but by $t = 100$ s (figure 14 *h*) the isotherms have commenced to rebound baroclinically, forming a distinct core seiche.

Figure 8(*b*) shows the simulated temperature traces for the three measurement points, as well as a temperature trace for a fourth point located at midheight in the cavity (see figure 1*a*). From this latter point it can be clearly seen that the seiche period of the core is independent of that in the intrusion. The former has a period of approximately 150 s, over double the period of the intrusion seiche. These values can be accounted for by the respective density gradients in each. The intrusion seiche in the stratified cavity is weaker than it was in the reference case. This is clearly shown by the reduced amplitude of centreline Nusselt-number oscillations in figure 9(*b*).

The experimental temperature traces have also been overlayed on figure 8(*b*). The agreement between experiment and simulation is clearly better than for the reference case in figure 8(*a*). It is not surprising, however, that there is not better agreement. Nothing is known of the actual stratification in the experiments, and so the case simulated is just one of an infinite number of possible stratifications. What is encouraging, however, is that the imposition of the stable gradient significantly changes the simulated response at the measurement points, both in respect to the rate of temperature increase and the overall temperatures attained during the measurement period.

A point worth noting is that the use of a stable, vertical temperature gradient has previously been advanced as a means of reducing convection associated with oscillatory response in side-heated cavities (Ostrach & Raghavan 1979). This behaviour has been observed in the growing of crystals from liquid metals (see, for example, Hurle, Jakeman & Johnson 1974). The present result clearly demonstrates a counterexample, i.e. there is a parameter range within which convection in regions of a cavity may be dramatically increased when such a gradient is present.

6. Conclusions

6.1. *Characteristics of the flow*

The basic flow examined in this paper was that produced by the side heating and cooling of a square, water-filled cavity at a Rayleigh number of 2×10^9. At time $O(10\text{ s})$, boundary layers form along the vertical walls. High vorticity of both signs is produced there; however, the negative vorticity is confined to a very thin region along the boundaries. The fluid with positive vorticity tends to accumulate adjacent to the emergent corners, where it can exert a direct influence on the intrusions that form and on the core of the cavity. Temperature stratified intrusions of relatively warm (cool) fluid propagate horizontally across the top (bottom) of the cavity after time $O(10^2\text{ s})$, producing as they advance, eddies of positive vorticity in the core of the cavity. Seiches form in the intrusions, as a result of the blocking effect of the opposite sidewall, and the fluctuating velocities these produce dominate heat transfer rates away from the boundaries. The seiches are damped within a few periods. Steady state occurs after time $O(10^3\text{ s})$. The approach to it takes the form of the filling of the cavity with a vertical temperature gradient.

For the spanwise aspect ratio considered (0.83) the flow on the symmetry plane is only slightly influenced by three-dimensional effects over the time considered in detail in this paper, confirming the relevance of the two-dimensional simulations. However, away from the symmetry plane, the flow is distinctly three-dimensional and characterized by recirculation zones and vortices.

The superposition of a stable vertical temperature stratification has a pronounced influence on the flow. For vertical gradients as low as $\frac{1}{100}$ the strength of the mean horizontal gradient, baroclinic production of vorticity results in the formation of a distinct core eddy, rotating in a sense that is up the cold side and down the warm side of the cavity. Though this flow is visually very dramatic, it has only a small influence on heat transfer rates across the centreline of the cavity which are by and large controlled by the velocity in the intrusions. In situations where mass transfer in the core is a consideration, this process may assume more importance. The steady-state condition is unaffected by the initial stratification.

6.2. *Validity of the scaling laws*

The general description and the scaling laws advanced by Patterson & Imberger (1980), for flows in regime V, appear to be well borne out by the results presented. The most contentious issue, the oscillatory approach to steady state, clearly holds. However, there are aspects that do not conform to the scaling. Most noticeable of these is the large transition in the intrusion width. Several mechanisms could account for it; however further experimental measurements will be needed to reach a definite conclusion.

6.3 *Comparison with experiment*

The single laboratory experiment that relates to this work agrees with many of the numerical results described above. Though the temperature measurements did not suggest the existence of a seiche within the intrusion, the numerical results have (with the advantage of hindsight) shown that this is directly attributable to an unfortunate choice of sampling positions.

The main point over which substantial disagreement exists is the experimental observation of a single core eddy with negative vorticity. The theoretical considerations presented suggest no mechanism for the generation of such vorticity in the core of an initially homogenous cavity, a fact borne out by the numerical simulations. Only when a weak vertical stratification is present do both theory and numerics agree with the observation. The fact that the imposition of such an initial condition also provides for far better agreement with temperature measurements lends credence to the hypothesis. Insofar as the degree of stratification required could readily be imparted by the absence of bottom insulation, overhead lighting or a stratification in the laboratory itself, this result highlights the difficulty inherent in conducting experiments of transient flows.

S.G.S. and R.L.S. acknowledge the support of the Division of Engineering and Geosciences, Office of Basic Energy Sciences, Department of Energy, USA through contracts No. DOE-DE-AT03-81ER10867 and DOE-DE-FG03-84ER13240. J.C.P. acknowledges the support of the Australian Research Council through Grant No. A48615453. This work was commenced during R.L.S.'s sabbatical leave at the University of Western Australia through support by the Queen's Fellowship Scheme, Department of Science, Australia. We wish to thank C. Y. Perng for his work on the code development, and the reviewers of an earlier draft for some insightful comments. Discussions with J. R. Koseff and S. G. Monismith helped clarify our understanding of this flow.

REFERENCES

BATCHELOR, G. K. 1954 Heat transfer by free convection across a closed cavity between vertical boundaries at different temperatures. *Q. Appl. Maths* **12**, 209–2233.

ELDER, J. W. 1965 Turbulent free convection in a vertical slot. *J. Fluid Mech.* **23**, 99–111.

FREITAS, C. J., STREET, R. L., FINDIKAKIS, A. N. & KOSEFF, J. R. 1985 Numerical simulation of three-dimensional flow in a cavity. *Intl J. Num. Methods Fluids* **5**, 561–575.

GILL, A. E. 1966 The boundary layer regime for convection in a rectangular cavity. *J. Fluid Mech.* **26**, 515–536.

GILL, A. E. & DAVEY, A. 1969 Instabilities of a buoyancy-driven system. *J. Fluid Mech.* **35**, 775–798.

HENDERSON, F. M. 1966 *Open Channel Flow.* Macmillan. 522 pp.

HURLE, D. T. J., JAKEMAN, E. & JOHNSON, C. P. 1974 Convective temperature oscillations in molten gallium. *J. Fluid Mech.* **64**, 565–576.

IVEY, G. N. 1984 Experiments on transient natural convection in a cavity. *J. Fluid Mech.* **144**, 389–401.

KOSEFF, J. R. & STREET, R. L. 1984 On end wall effects in a lid-driven cavity flow. *Trans. ASME* I: *J. Fluids Engng* **106**, 385–389.

LEONARD, B. P. 1979 A stable and accurate convective modeling procedure based on quadratic upstream interpolation. *Comput. Methods Appl. Mech. Engng.* **19**, 59–98.

MALLINSON, G. D. & DE VAHL DAVIS, G. 1977 Three-dimensional natural convection in a box: a numerical study. *J. Fluid Mech.* **83**, 1–31.

MCGUIRK, J. J., TAYLOR, A. M. K. P. & WHITELAW, J. H. 1982 The assessment of numerical diffusion in upwind difference calculations of turbulent recirculating flows. In *Turbulent Shear Flows*, Vol. 3 (ed. L. J. S. Bradbury *et al.*). Springer.

MORTON, B. R. 1984 The generation and decay of vorticity. *Geophys. Astrophys. Fluid Dyn.* **28**, 277–308.

OSTRACH, S. & RAGHAVAN, C. 1979 Effect of stabilizing thermal gradients on natural convection in rectangular cavities. *Trans. ASME* C: *J. Heat Transfer* **101**, 238–243.

PATANKAR, S. V. 1980 *Numerical Heat Transfer and Fluid Flow.* McGraw-Hill. 289 pp.

PATTERSON, J. C. 1984 On the existence of an oscillatory approach to steady natural convection in cavities. *Trans. ASME* C: *J. Heat Transfer* **106**, 104–108.

PATTERSON, J. C. & IMBERGER, J. 1980 Unsteady natural convection in a rectangular cavity. *J. Fluid Mech.* **100**, 65–86.

PERNG, C. Y. & STREET, R. L. 1988 Three-dimensional unsteady flow simulations: alternative strategies for a volume-averaged calculation. *Intl J. Num. Methods Fluids* (in press).

PRASAD, A. K., PERNG, C. Y. & KOSEFF, J. R. 1988 Some observations on the influence of longitudinal vortices in a lid-driven cavity flow. *AIAA/ASME/SIAM/APS 1st National Fluid Dynamics Congress July 25–28, 1988*, *Cincinnati*, *Ohio*, pp. 288–295.

TABACZYNSKI, R. S., HOULT, D. P. & KECK, J. C. 1970 High Reynolds number flow in a moving corner. *J. Fluid Mech.* **42**, 249–256.

TURNER, J. S. 1973 *Buoyancy Effects in Fluids*. Cambridge Universtiy press. 368 pp.

VAN DOORMAAL, J. P. & RAITHBY, G. D. 1984 Enhancements of the SIMPLE Method for predicting incompressible fluid flows. *Numer. Heat Transfer* **7**, 147–163.

WORSTER, M. G. & LEITCH, A. M. 1985 Laminar free convection in confined regions. *J. Fluid Mech.* **156**, 301–319.

YEWELL, R., POULIKAKOS, D. & BEJAN, A. 1982 Transient natural convection experiments in shallow enclosures. *Trans. ASME* C: *J. Heat Transfer* **104**, 533–538.